Rotational channel interactions of vibrationally excited *np* Rydberg states of the triatomic hydrogen molecule

R. Reichle, I. Mistrík, U. Müller, and H. Helm
Fakultät für Physik, Universität Freiburg, Hermann-Herder-Strasse 3, D-79104 Freiburg, Germany
(Received 11 May 1999)

We have carried out a precise measurement of the wavelength dependence of the two-step photoionization cross section of triatomic hydrogen via the $3s\ ^2A_1'$ Rydberg state at energies beyond the ionization limits that belong to the first symmetric-stretch excited vibrational state $\{1,0^0\}$ of the ion core. In this energy region, rotational and vibrational channel couplings due to the interaction between the outer *p* electron and the H_3^+ core are expected. We find strong coupling between the two *p* series with total angular momentum $N=2$ which converge to the rotational levels $N^+=1$ and 3 of the underlying $H_3^+\{1,0^0\}$ core. Surprisingly, regular perturbations are also detected in the symmetric-stretch-excited $N=1$ *p* series. Rydberg levels of the $ndE'\ \{1,0^0\}$ series are identified as the perturbing channel. This implies a change in the orbital angular momentum of the Rydberg electron during the short-range interaction. The experimental spectra are analyzed in two-channel quantum-defect models. Eigenchannel quantum defects, coupling constants, and transition moment ratios are determined and compared to the results of recent *ab initio* calculations. [S1050-2947(99)06611-1]

PACS number(s): 33.80.Rv, 33.80.Eh

I. INTRODUCTION

The H_3 molecule plays the role of a prototype for a polyatomic molecule. Its electronic structure is the simplest possible for a triatomic neutral species making comparisons between experimental and *ab initio* theoretical treatments feasible. On the other hand, the rotational and vibrational degrees of freedom which are characteristic of heavier systems are fully developed in H_3. The triatomic hydrogen molecule is often used to study fundamental aspects of the dynamics on the repulsive ground-state potential surface which can be considered as the simplest possible chemical reaction path between neutral particles [1,2]. Further significance of H_3 comes from astrophysics where the dissociative recombination process of H_3^+ ions with electrons plays an important role [3–5]. Quite late in the history of molecular physics, the triatomic hydrogen molecule was discovered by Herzberg's group in emission from a hydrogen discharge plasma [6–10]. These studies covered the lowest ($n=2$ and 3) Rydberg states and determined the molecular constants of these states.

The neutralized ion-beam technique first applied by Devienne [11] and Gellene and Porter [12] exploits the metastability of the H_3 $2p\ ^2A_2''(N=K=0)$ level for producing long-lived H_3 molecules in a fast neutral beam. A theoretical symmetry analysis confirmed that the $2p\ ^2A_2''(N=K=0)$ level is the only candidate for a metastable state with a low principal quantum number [13]. The first observations of Rydberg states with a high principal quantum number were made by Helm [14]. In a series of papers, different aspects of H_3 were studied in photoionization experiments [14,15] covering *s* and *d* series with different core excitations. The corresponding ionization limits and quantum defects were measured for the first time. Depletion spectroscopy was applied to explore the nature of low-lying Rydberg states and to determine their vibrational frequencies [16]. Photodissociation of H_3 was studied using time- and position-sensitive detectors [17]. Since the *p* and *f* series are inaccessible in one-photon excitation from the metastable $2p\ ^2A_2''(N=K=0)$ state, two-step excitation experiments followed [18,19]. Not unexpected interactions between the ion core and the valence electron were found to be stronger in the *p* series than the *f* series. This can be understood from the fact that a low angular momentum electron penetrates deeper into the ion core and, therefore, the short-range interaction is much stronger. The analysis of the *p* series for total angular momentum $N=2$ was performed with two-channel quantum-defect theory with reasonably good agreement. Deviations in the intensity profile of the Rydberg series were attributed to vibrational interactions [19].

A full multichannel quantum-defect theory (MQDT) calculation using rovibrational frame transformation and *ab initio* quantum-defect surfaces [20] was performed by Stephens and Greene [21] in a model including 40 rovibronic channels. Good agreement with the spectrum measured by Bordas and Helm [19] in the vicinity of the lowest ionization threshold was achieved in the discrete region as well as in the Beutler-Fano region. In addition, this model was able to assign a number of vibrationally autoionizing levels in the open continuum as well as interlopers in the Beutler Fano region. A most striking result of their study [21] was the finding that the Jahn-Teller effect plays an essential role in the autoionization process of H_3.

This paper deals with an investigation of *np* Rydberg series converging to vibrationally excited core states of the lowest symmetric-stretch mode. A two-channel analysis is performed to determine the line positions and intensities, quantum defects, and coupling strengths for the series with $N=1$ and 2 angular momenta. In addition to the strong rotational coupling among *p* Rydberg series, evidence is found for rotationally induced coupling between electronic *p* and *d* states in H_3.

II. EXPERIMENT

The Freiburg neutral beam photoionization spectrometer shown in Fig. 1 was recently used to investigate Rydberg

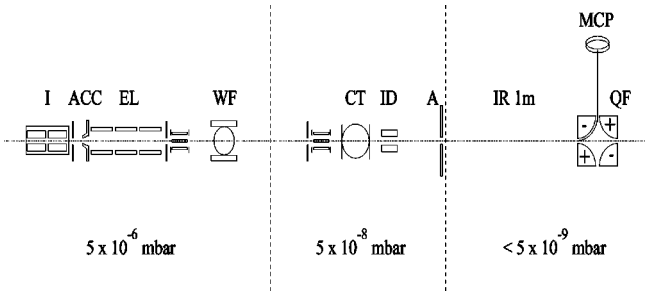

FIG. 1. Schematic of the Freiburg neutral beam photoionization spectrometer. I: hollow cathode discharge ion source; ACC: ion-beam extraction and acceleration stage; EL: einzel lens; WF: Wien filter; CT: charge-transfer cell; ID: ion deflector; A: aperture; IR: laser-interaction region; QF: electric quadrupole ion deflector; MCP: microchannel plate detector.

states of the D_3 molecule [22], and is only briefly discussed here. Triatomic hydrogen ions are produced in a hollow cathode discharge in hydrogen. The ions are extracted by an electric field, accelerated to an energy of 3.6 keV, focused by an einzel lens and mass selected by a Wien filter. The H_3^+ current is about 100 nA after mass selection and the intensity ratio of H_3^+, H_2^+, and H^+ currents is typically 10:1:1. The electrodes of the discharge tube are cooled by liquid nitrogen which significantly increases the population in the H_3^+ rovibrational ground state. The H_3^+ beam is partially neutralized (10–30 %) by near-resonant charge transfer in cesium. After the charge-transfer cell, the residual ions are removed from the neutral beam by an electric field, which also serves to quench by field ionization the small abundance of high principal quantum number Rydberg states formed by charge transfer. Neutral products of dissociative charge transfer are intercepted by an aperture of 1 mm diameter located 35 cm downstream of the charge-transfer cell. H_3 molecules in the metastable state $2p\ ^2A_2''(N=K=0)$ which survive the travel from the charge-transfer cell to the aperture are excited by counter propagating laser beams in the 1-m-long interaction region. H_3^+ ions created in the interaction region by photoexcitation of autoionizing H_3 states are energy-selected by a quadrupole field and deflected to a multichannel plate detector which is operated in pulse-counting mode. A gated dual counter (200 MHz) is used to accumulate the signals produced by the laser pulses and the background events separately. These data are then transferred to a laboratory computer and stored for further treatment. Two dye lasers pumped by an excimer laser are operated in the visible spectral range. An optical delay line is adjusted for both pulses to overlap in time in the interaction region. The dye lasers are programmed and scanned under control of the laboratory computer. The calibration procedure of the laser wavelength is similar to that applied in a previous investigation [22] using an optogalvanic cell filled with argon or neon. For calibration in the far-red spectral range, a rubidium absorption cell is employed. The accuracy of the wavelength calibration is 0.15 cm^{-1}. The bandwidth of each laser is 0.20 cm^{-1}.

III. TWO-STEP PHOTOIONIZATION SCHEME

The two-step laser-excitation scheme applied in our experiment is shown in Fig. 2. The wavelength of one of the

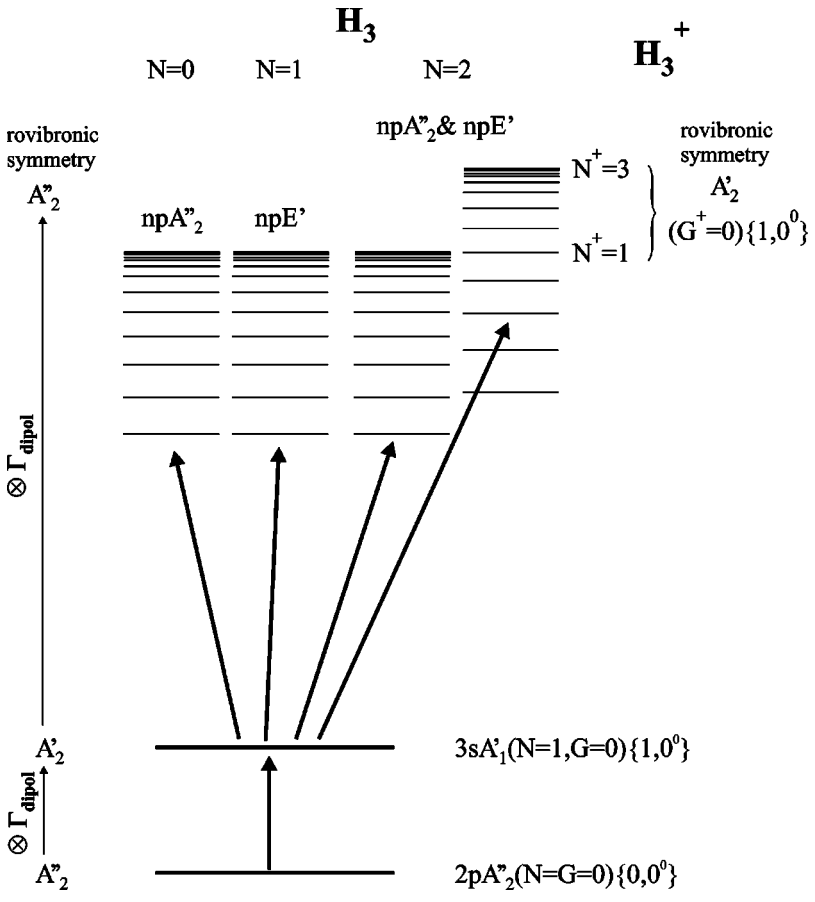

FIG. 2. Energy-level scheme of the vibrationally symmetric-stretch-excited H_3 np Rydberg series accessible via the H_3 $3s\ ^2A_1'(N=1, G=0)\{1,0^0\}$ intermediate state. The H_3 Rydberg states with total angular momenta $N=0$, 1, and 2, accessed in the two-step laser-excitation experiment, are shown along with their rovibronic and electronic symmetry species. The angular momenta and symmetry labels of the underlying H_3^+ core levels are also shown.

TABLE I. Rovibronic symmetries of the states relevant for two-step photoionization of H_3 via the $3s\ ^2A_1'(1,0)\{1,0^0\}$ intermediate state. States with total angular momentum $N=0$, 1, and 2 and $G=3t$, with $t=0,1,2,\ldots$ are listed.

H_3^+ core[a]	Energy[b]	$\Gamma_{H_3^+}$	Threshold[c]	Rydberg electron[d]	N	G	final state Γ_f
$(1,0)\{0,0^0\}$	86.935	A_2'	9655.04	$L=0$ (ns), A_1'	1	0	A_2'
$(2,3)\{0,1^1\}$	2613.874	A_2'	12 181.98	$L=1$ (np), A_1''	1,2	3	A_2''
$(3,3)\{0,1^1\}$	2876.520	A_2'	12 444.63	$L=1$ (np), A_1''	2	3	A_2''
$(1,0)\{1,0^0\}$	3262.997	A_2'	12 831.10	$L=1$ (np), A_1''	0,1,2	0	A_2''
$(3,0)\{1,0^0\}$	3682.472	A_2'	13 250.58	$L=1$ (np), A_1''	2	0	A_2''

[a]Quantum numbers: $(N^+,\ G^+)\{\nu_1,\nu_2^{l_2}\}$.
[b]Core energies in cm^{-1} from Ref. [25], relative to the minimum of the H_3^+ potential energy surface.
[c]Ionization threshold in cm^{-1} above the $3s\ ^2A_1'(1,0)\{0,0^0\}$ state. The values are calculated using the energy values 29 562.14 cm^{-1} for the $H_3^+(1,0)\{0,0^0\}$ threshold [26,37] above $2p\ ^2A_2''(0,0)\{0,0^0\}$, and 19 907.1 cm^{-1} for the $3s\ ^2A_1'(1,0)\{1,0^0\}$ level [23] above the $2p\ ^2A_2''(0,0)\{0,0^0\}$ metastable state.
[d]Angular momentum L and symmetry label Γ_L of the Rydberg electron in Hund's case (d) basis.

lasers is fixed to excite the vibrationally nondiagonal transition from the metastable $2p\ ^2A_2''$ state to the symmetric-stretch excited $3s\ ^2A_1'$ state of H_3. At high laser intensity, 1+1-photon resonance-enhanced multiphoton ionization (REMPI) via this state [23] is used to select the wavelength setting of the first laser. With the first laser at low intensity ($\leqslant 200\ \mu J$) the second laser is tuned to excite *p*-type Rydberg states converging to the lowest orthorotational levels of symmetric-stretch excited H_3^+. The states involved in this excitation scheme and their symmetries are discussed in the following.

In Hund's case (b), the projection, λ, of the outer electron angular momentum L on the molecular symmetry axis is a constant of motion. The electronic states are characterized by the electronic symmetry Γ_e. For *p* states with $L=1$, the electronic symmetries are A_2'' and E' for $\lambda=0$ and $\lambda=1$, respectively. The vibrational states are classified by the quantum numbers ν_1 and ν_2 of the symmetric stretch and degenerate vibrational modes, and by the vibrational angular momentum l_2. In addition, the total angular momentum apart from electron spin N and it's projection K on the molecular symmetry axis are required to characterize a rovibronic level. For the discussion of symmetries, it is convenient to use Hougen's quantum number $G=|\lambda+l_2-K|$ [24,13]. In the following, we use the notation $(N,G)\{\nu_1,\nu_2^{l_2}\}$ to label the rovibronic states of H_3. For G assuming zero or integer multiples of 3, the nuclear spins of the protons are coupled to $I_{\text{total}}=3/2$ (ortho levels). For all other values of G, the total nuclear spin is $I_{\text{total}}=1/2$ (para levels) [13]. The states of H_3^+ are labeled by the same notation as those of H_3, with additional $^+$ superscripts attached to the quantum numbers if required for clarity. The vibrationless $2p\ ^2A_2''(0,0)\{0,0^0\}$ metastable state of H_3, which serves as the initial state in our two-step laser-excitation experiments, is an ortho level ($G=0$). In optical dipole transitions, the total nuclear spin is conserved. The quantum numbers G of all levels accessible by laser excitation of the metastable level must be integer multiples of 3 ($G=3t$ with $t=0,1,2\ldots$).

As discussed by Lembo *et al.* [23], a Hund's case (d) model is more convenient for the description of high principal quantum number Rydberg states. The angular part of the Rydberg electron wave function in the molecular frame $Y_{L\lambda}(\hat{r})$ is expressed in a space-fixed frame by

$$Y_{Lm}(\hat{r}')=\sum_{\lambda} D_{\lambda m}^{(L)*}(R'\leftarrow R)Y_{L\lambda}(\hat{r}),$$

where primed coordinates refer to the laboratory coordinate system, and unprimed coordinates to the molecule-fixed coordinate system [Ref. [21], Eq. (18)]. An inspection of the wave function $Y_{Lm}(\hat{r}')$ shows that the symmetry of the Hund's case (d) Rydberg electron in the D_{3h} group is A_1' for L even and A_1'' for L odd. Following Hougen [24] the symmetry of the dipole operator $\Gamma_d=\Gamma_{T_z}\otimes\Gamma_{R_z}$ is the direct product of the species of the translation along the *z* axis (Γ_{T_z}) and the rotation about the *z* axis (Γ_{R_z}). In the D_{3h} symmetry group, we find that the symmetry of the dipole operator is $\Gamma_d=A_1''$. From the $2p\ ^2A_2''(0,0)\{0,0^0\}$ initial state having A_2'' rovibronic symmetry, states with $A_2''\otimes A_1''=A_2'$ symmetry can be excited in single-photon transitions. In the first excitation step, we have chosen to prepare the $3s\ ^2A_1'(1,0)\{1,0^0\}$ state in a vibrationally nondiagonal transition (see Fig. 2). This intermediate state can be viewed as an *s* Rydberg electron attached to a vibrationally symmetric-stretch excited $H_3^+(1,0)\{1,0^0\}$ ion core. The A_2' overall symmetry label of this state results from a direct product of the A_1' electronic symmetry of the *s* electron with the A_2' rovibronic symmetry of the H_3^+ core $1s^2(1,0)\{1,0^0\}$. The rovibronic symmetry of the final states accessible in the second excitation step is $A_2'\otimes A_1''=A_2''$. From the $N=1$, $G=0$ intermediate state, final states with total angular momentum $N=0$, 1, and 2 are accessible in one-photon transitions. Additionally, the quantum number G must be zero or an integer multiple of 3. For *p*-type final states having electronic angular momentum $L=1$ and A_1'' electronic symmetry in the laboratory frame, the ion core symmetry has to be $\Gamma_{H_3^+}=A_2'$. On the other hand, for *s* and *d* Rydberg electrons ($\Gamma_{L=0,2}=A_1'$), ion cores with symmetry $\Gamma_{H_3^+}=A_2''$ are required.

The accessible final states constructed in the Hund's case (d) frame by attaching *p*-Rydberg electrons to H_3^+ core states are listed in Table I. The possible core states are

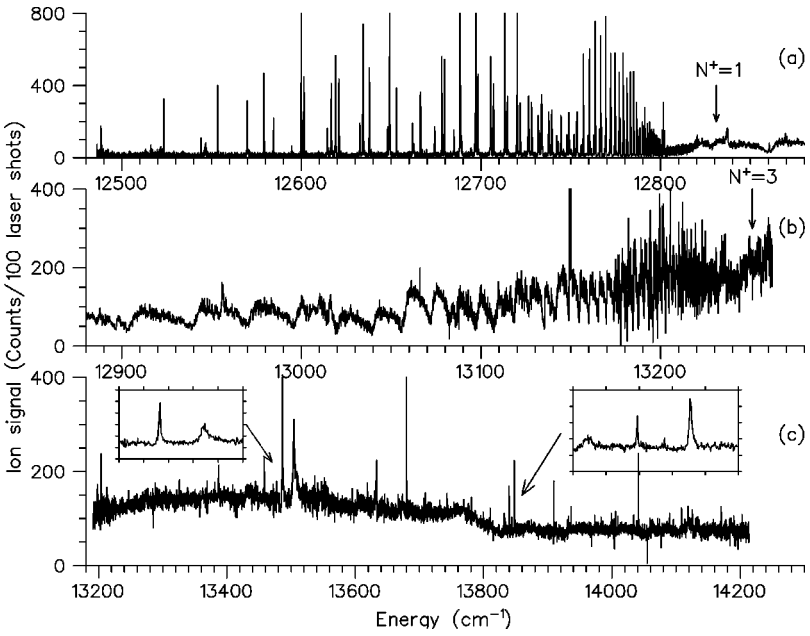

FIG. 3. Photoionization spectra of H_3 via the $3s\ ^2A_1'(N=1,\ G=0)\{1,0^0\}$ intermediate state. The measurements cover the 12 490 to 14 200 cm^{-1} energy region above the $3s\ ^2A_1'(N=1,\ G=0)\{1,0^0\}$ state. The ionization limits ($N^+=1$, $G^+=0$) and ($N^+=3$, $G^+=0$) of symmetric-stretch-excited $H_3^+\{1,0^0\}$ are indicated by arrows. The spectrum is separated into a ''discrete'' part (a), the Beutler-Fano region (b), and the pure continuum (c). The insets in the lower part of the figure show the resonances in the continuum in the energy regions 13 470–13 520 and 13 830–13 855 cm^{-1}, respectively.

($N^+=1,3$, $G^+=0$) if no ν_2 vibration is excited and ($N^+=2,3$, $G^+=3$) for one quantum of bending mode excitation. The energies of the H_3^+ levels listed in Table I are the results of highly accurate *ab initio* calculations by R. Jaquet *et al.* [25]. The ionization thresholds listed in Table I are determined using the value of 29562.14 cm^{-1} for the first ionization limit of the $2p\ ^2A_2''(0,0)\{0,0^0\}$ state to the $H_3^+(1,0)\{0,0^0\}$ core measured by Ketterle *et al.* [26], and the value of 19907.1 cm^{-1} for the $2p\ ^2A_2''\rightarrow 3s\ ^2A_1'(1,0)\{1,0^0\}$ excitation frequency measured by Lembo *et al.* [23].

In Fig. 2, the final states of the *p* series with symmetric-stretch vibrational excitation are shown in a schematic level scheme. The electronic symmetries in the Hund's case (b) limit are A_2'' and E' for $N=0$ and 1, respectively. For the $N=2$ series converging to each, ($N^+=1$, $G^+=0$) and ($N^+=3$, $G^+=0$), A_2'' as well as E' electronic symmetries are allowed, which leads to strong rotational coupling between these series.

IV. EXPERIMENTAL RESULTS

In Fig. 3, the two-step photoionization spectrum of H_3 via the $3s\ ^2A_1'(1,0)\{1,0^0\}$ intermediate state is shown. The measurement covers the energy range between 12 490 and 14 200 cm^{-1} relative to the intermediate state. The final-state energy is in the range from 351–564 meV above the lowest ionization threshold, encompassing the first symmetric-stretch excited level of H_3^+ at 394 meV. The power of the laser pulse exciting the $2p\ ^2A_2''\rightarrow 3s\ ^2A_1'$ transition was attenuated to minimize the background from resonance-enhanced multiphoton ionization (1+1 REMPI). The energies of the lowest ortho levels ($N^+=1$, $G^+=0$), and ($N^+=3$, $G^+=0$) of H_3^+ with one quantum of symmetric-stretch excitation $\{1,0^0\}$ are indicated by arrows in Fig. 3. The spectrum consists of three distinct regions. Below the ($N^+=1$, $G^+=0$) limit, discrete lines dominate. These transitions appear in the spectrum due to autoionization to the lowest vibrational level of the ion. In the so-called Beutler-Fano region between the ($N^+=1$, $G^+=0$) and ($N^+=3$, $G^+=0$) limits, we find a regularly structured continuum. Above the ($N^+=3$, $G^+=0$) limit, an almost structureless continuum is observed with strong resonances superimposed. Their asymmetric line profiles (Fano profiles [27]) are due to mixing of H_3 states having higher vibrational excitation with the open continua. Although the spectra shown in Fig. 3 are corrected for the dark count rate of the detector, a small, continuous background is found in the ''discrete'' part below the first vibrationally excited threshold. This background is due to direct ionization into the underlying continua built on vibrationless or degenerate mode excited H_3^+ cores, $\{0,0^0\}$ and $\{0,1^1\}$, and extends into the Beutler-Fano region and the pure continuum. For all final states in the energy region covered in Fig. 3, vibrational autoionization is an open ionization mechanism which leads to slightly asymmetric line shapes of the resonances.

The ''discrete'' part and the Beutler-Fano region of the spectrum can be understood from the level scheme in Fig. 2. The respective state energies are listed in Table I. Four *p* Rydberg series with total angular momenta $N=0$, 1, and 2 can be formed from ($N^+=1$, $G^+=0$) and ($N^+=3$, $G^+=0$) H_3^+ cores. The two series with $N=2$ are coupled by pure rotational interaction. This coupling is the origin of the modulation of the ion yield in the Beutler-Fano region as well as perturbations of the line positions and intensity modulations in the ''discrete'' part of the spectrum. Within the subset of states converging to ($N^+=1$, $G^+=0$), the series with $N=0$ and 1 are expected to be unperturbed.

The final-state angular momentum is further restricted by the relative orientation of the polarization vectors of the two excitation lasers. For parallel polarizations, only $N=0$ and 2, for perpendicular polarizations only $N=1$ and 2 states [21] can be excited. By combining measurements with different laser polarizations, we determine the final-state angular momenta of the discrete lines. Measurements in the 12 750–12 780 cm^{-1} region of the discrete spectrum with parallel and perpendicular orientation of the electric vectors of the laser fields are shown as (a) and (b) in Fig. 4. Lines appear-

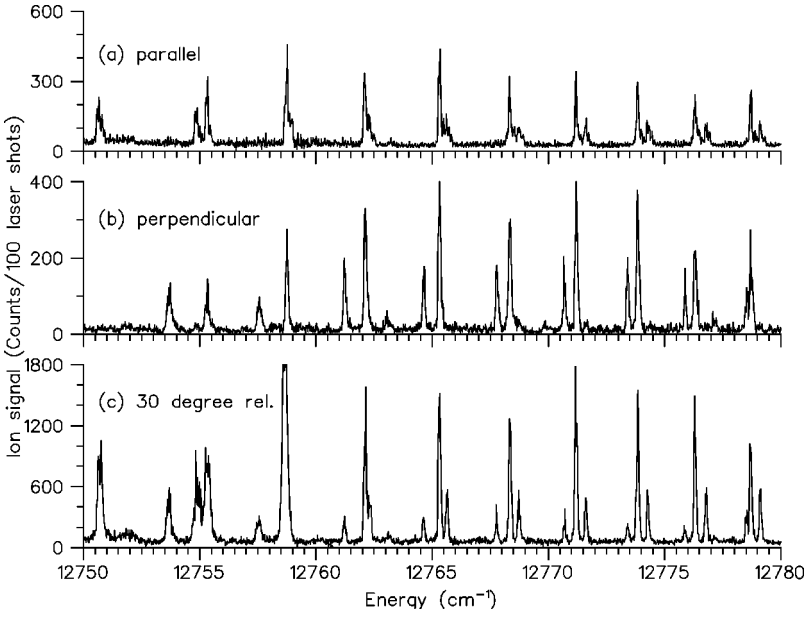

FIG. 4. Experimental determination of the final-state total angular momentum N by changing the orientation of the laser polarization directions. The two-step photoionization spectrum of H_3 in the 12 750–12 780 cm^{-1} energy region above the $3s\ ^2A_1'(N=1, G=0)\{1,0^0\}$ intermediate state is shown. The electric vectors of the two laser fields were oriented parallel in spectrum (a) and perpendicular in spectrum (b) with respect to each other. Spectrum (c) was recorded with a 30° relative orientation of the laser polarization vectors. Spectrum (a) contains lines with only $N=0$ and 2. Spectrum (b) contains only lines with $N=1$ and 2. Spectrum (c) corresponds to an incoherent superposition of spectra (a) and (b).

ing in the spectra with parallel [Fig. 4(a)] as well as with perpendicular [Fig. 4(b)] polarization must have $N=2$ final-state angular momentum. Lines appearing only in the measurement with parallel polarization [Fig. 4(a)] belong to Rydberg series with $N=0$, those appearing only in the measurement with perpendicular polarization [Fig. 4(b)] have $N=1$.

A third measurement was carried out with an angle of 30° between the polarization vectors of the two photons. The resulting spectrum [Fig. 4(c)] is an incoherent superposition of the parallel and perpendicular spectra and contains lines with $N=0$, 1, and 2. We determined the excitation frequencies of the discrete lines by fitting Gaussian functions to the measured spectra. The two series with $N=2$ are strongly mixed, and the transition frequencies could not be fitted by a simple Rydberg formula. A two-channel quantum-defect theory was used to evaluate the data as we discuss in the following.

V. THEORETICAL CONSIDERATIONS

In order to simulate the observed spectra, we follow the formalism of Fano [28]. The H_3 molecule is viewed as a H_3^+ core with an additional valence electron attached to it. The two inner electrons fill the $(1sa_1')$ molecular orbital forming a closed shell. For large distances of the valence electron, the electric field of the nuclei is shielded to that of a single positive elementary charge. Only at very small distances, the motion of the valence electron is influenced by the structure and the properties of the ion core. This leads to an L-uncoupling effect which was described theoretically by Pan and Lu [29] by the introduction of two different basis sets. The close-coupling or eigenchannel basis is appropriate for small distances of the electron from the core and for low principal quantum numbers n. In this case, the valence electron is strongly coupled to the symmetry axis of the H_3^+ ionic frame. The projection λ of the valence electron angular momentum L onto the molecular figure axis is a good quantum number [Hund's case (a/b), if electron spin is neglected]. With increasing distance, the motion of the valence electron separates from the core motion [Hund's case (d) limit], and the quantum number N^+ of the core angular momentum becomes a good quantum number. In this so-called ionization basis, the total energy E of the system can be written as the sum of the rovibronic energy $I_{\rm ion}$ of the H_3^+ core and the energy W of the Rydberg electron:

$$E=I_{\rm ion}+W, \quad W=-\frac{R}{\nu^2}. \tag{1}$$

Herein $R=109\,717.405\ cm^{-1}$ represents the Rydberg constant for H_3 calculated using the reduced mass of the $H_3^+ + e^-$ system. The eigenvalue spectrum of E is determined by the effective quantum number $\nu=n-\mu$, which can be written by an integer n and the nearly energy-independent quantum defect μ.

A. Single-channel quantum-defect theory

In a system consisting of a spherically symmetric ion core and a single valence electron, e.g., an alkali atom, the potential $V(r)$ depends only on the distance r of the valence electron from the center of the core. The wave function separates into angular and radial parts. The radial Schrödinger equation is given by

$$\frac{\hbar^2}{2\mu}\frac{\partial^2\rho(W,r)}{\partial r^2}+\left(W-V(r)-\frac{\hbar^2 l(l+1)}{2\mu r^2}\right)\rho(W,r)=0 \tag{2}$$

with the total energy W and the angular momentum l of the valence electron. The solution $\rho(W,r)=r\mathcal{R}(W,r)$ is the product of the distance r with the radial wave function $\mathcal{R}(W,r)$. The second-order differential equation has two independent solutions for each potential.

For a pure Coulomb potential [31], these solutions are the regular and irregular Coulomb functions $f(\nu,l,r)$ and $g(\nu,l,r)$ with the parameter $\nu=\sqrt{-R/W}$. The Coulomb functions are known analytically. They oscillate in the classically allowed region of the potential with a phase shift of

90° with respect to each other [32]. The asymptotic behavior of the Coulomb functions for $r \to 0$ are

$$\lim_{r\to 0} f(r) \sim r^{l+1}, \quad \text{regular},$$
$$\lim_{r\to 0} g(r) \sim r^{-l}, \quad \text{irregular}, \tag{3}$$

independent of W, and in the limit $r \to \infty$,

$$f(r) \to u(\nu,l,r)\sin \pi\nu - v(\nu,l,r)\cos \pi\nu,$$
$$g(r) \to -u(\nu,l,r)\cos \pi\nu - v(\nu,l,r)\sin \pi\nu \tag{4}$$

for $W<0$. For large r, the functions $u(\nu,l,r)$ and $v(\nu,l,r)$ are exponentially increasing and decreasing, respectively.

For $W<0$, the general solutions $\rho(W,r)$ of the radial Schrödinger equation (2) are linear combinations of $f(\nu,l,r)$ and $g(\nu,l,r)$. The solutions which are physically meaningful have to remain finite at the origin $(r \to 0)$ and to vanish sufficiently fast at large distances $r \to \infty$. For bound states $(W<0)$, these requirements lead to a discrete spectrum of eigenvalues W. For the pure Coulomb potential, only the regular Coulomb function $f(r)$ remains finite at the origin. The additional condition

$$\sin \pi\nu = 0 \tag{5}$$

has to be fulfilled to cancel the exponentially increasing part [function $u(\nu,l,r)$] at large r. As a consequence, the values of the parameter ν are integers n and the energy spectrum is discrete with $W=-R/n^2$. For $W>0$, the asymptotic solutions for $r \to \infty$ are outgoing waves having oscillatory character [31].

The potential $V(r)$ contains the attraction by the nuclei as well as the repulsion by the inner-shell electrons. The deviations from a pure Coulomb potential result from the finite size of the ion core. In the following, we assume that the potential $V(r)$ outside of a sphere with radius r_0 can be approximated to high accuracy by a Coulomb potential. Within the sphere (short-range interaction zone), the shielding of the nuclear charge by the inner-shell electrons vanishes, and the potential becomes deeper than that of a single charge. The wave functions $\rho(W,r)$ for $V(r)$ outside of the interaction zone differ from those of the pure Coulomb potential only by a nearly energy-independent phase shift $\pi\mu$, and can be constructed by a linear superposition of regular and irregular Coulomb functions:

$$\rho(W,l,r) = f(\nu,l,r)\cos \pi\mu - g(\nu,l,r)\sin \pi\mu. \tag{6}$$

The value of μ is chosen to join $\rho(W,r)$ smoothly to the exact solutions inside the short-range zone at the boundary $r=r_0$. According to Eqs. (4) and (6), the asymptotic form of $\rho(W,l,r)$ is

$$\lim_{r\to\infty} \rho(W,l,r) \sim u(\nu,l,r)(\sin \pi\nu \cos \pi\mu + \cos \pi\nu \sin \pi\mu)$$
$$- v(\nu,l,r)(\cos \pi\nu \cos \pi\mu + \sin \pi\nu \sin \pi\mu) \tag{7}$$

for large r. For stationary states $[W<0]$, the physically meaningful wave functions have to decrease sufficiently fast in the limit of large r. This condition can in general only be fulfilled if the coefficient of the exponentially increasing function $u(\nu,l,r)$ vanishes:

$$\sin(\pi(\nu+\mu)) = 0. \tag{8}$$

The argument $\nu+\mu=n$ has to assume integer values n yielding noninteger values of the effective quantum number ν and energy eigenvalues $W=-R/(n-\mu)^2$. The phase shift $-\pi\mu$ at $r=r_0$ corresponds to the quantum defect, and can be determined either empirically from experimental data or by *ab initio* calculations.

B. Frame transformation

In the case of H_3, the sets of good quantum numbers are $\alpha=(L,\lambda,G^+,N,M)$ in the close-coupling basis and $i=(L,N^+,G^+,N,M)$ in the ionization basis for high n. Here N is the total angular momentum, and M its projection onto a space-fixed axis. Instead of K^+, we use Hougen's quantum number $G^+=|l_2-K^+|$, which incorporates the vibrational angular momentum (note that λ^+ is zero for the electronic ground state of $H_3{}^+$). Pan and Lu derived the unitary frame transformation matrix $U_{i\alpha}$ between these two basis sets [29]. For the special case of a p Rydberg series with $L=1$ and $N=2$, the transformation matrix $U_{i\alpha}$ is given by

$$U_{i\alpha} = \begin{pmatrix} \sqrt{2/5} & \sqrt{3/5} \\ -\sqrt{3/5} & \sqrt{2/5} \end{pmatrix} = \begin{pmatrix} \cos\theta & \sin\theta \\ -\sin\theta & \cos\theta \end{pmatrix} \tag{9}$$

It can be expressed by a rotation matrix with the frame transformation angle $\theta=\arccos(\sqrt{2/5})$. In the following, this frame transformation matrix is used to extend the formulation of quantum-defect theory (QDT) to the multichannel problem (MQDT) where several coupled ionization channels are open (Fano [28]).

C. Multichannel quantum-defect theory

The properties of a molecular core (rotation and vibration) may lead to the existence of N ionization channels with individual ionization limits I_i. The solutions of the radial Schrödinger equation (2) for a total energy W are linear combinations of the regular and irregular Coulomb functions $f(\nu_i,l,r)$ and $g(\nu_i,l,r)$ with the effective quantum numbers ν_i defined by

$$W \equiv I_1 - \frac{R}{\nu_1^2} = \cdots = I_N - \frac{R}{\nu_N^2} \tag{10}$$

We can construct the ionization-basis wave functions Ψ_i

$$\Psi_i = \frac{1}{r}\chi_i[f(\nu_i,l,r)\cos(\pi\nu_i) + g(\nu_i,l,r)\sin(\pi\nu_i)]$$
$$i = 1,\ldots,N \tag{11}$$

for each ionization threshold I_i. The functions χ_i contain the angular- and spin-dependent parts of the wave functions. The wave functions [Eq. (11)] automatically fulfill the boundary

condition at large distance r. As discussed in Sec. V A, the boundary conditions at $r=r_0$ select the physically meaningful solutions. If the ionization channels are not interacting, an individual quantum defect is associated with each ionization channel. In general, the quantum numbers classifying the core states (ionization basis) are inappropriate for small r, as discussed in Sec. V B. To apply the boundary conditions, we have to switch to the eigenchannel basis. We construct eigenchannel wave functions using the transformation matrix $U_{i\alpha}$:

$$\Psi_\alpha=\frac{1}{r}\sum_i U_{i\alpha}\chi_i[f(\nu_i,l,r)\cos(\pi\mu_\alpha) - g(\nu_i,l,r)\sin(\pi\mu_\alpha)]. \quad (12)$$

The sum runs over all ionization channels i coupled by the transformation matrix $U_{i\alpha}$. The wave functions [Eq. (12)] allow us to introduce independent quantum defects μ_α for each element of the eigenchannel basis. These quantum defects can be determined empirically or by *ab initio* methods. In general, the wave functions Ψ are diagonal neither in the eigenchannel nor the ionization basis, and can be expanded in terms of the functions Ψ_α,

$$\Psi=\sum_\alpha B_\alpha\Psi_\alpha, \quad (13)$$

which allows a mixing of all eigenchannels. To fulfill the boundary condition at $r\to\infty$, the coefficients of the exponentially increasing functions $u(\nu_i,l,r)$ have to vanish. This leads to a system of equations

$$\sum_\alpha U_{i\alpha}\sin\pi(\nu_i+\mu_\alpha)B_\alpha=0, \quad (14)$$

which gives an implicit dependence of all effective quantum numbers ν_i and a mixing of all channels of the ionization basis. Nontrivial solutions of this system of linear equations (14) exist only if

$$\det(U_{i\alpha}\sin\pi(\nu_i+\mu_\alpha))=0. \quad (15)$$

Using the determinantal equation (15) together with the $N-1$ relations between the ν_i established by the Rydberg equations (10), the unknown ν_i can be determined exactly. They define the total energy W of the stationary states. Since Eq. (15) contains a periodic function, these equations yield a complete spectrum of energies W. Knowing ν_i, the amplitudes B_α can be determined by solving Eq. (14), and a complete set of wave functions for the stationary states can be constructed.

The model described above holds for the case of N closed channels, i.e., the total energy W is always below the lowest ionization limit. If the energy is increased beyond an ionization limit, the respective channel is said to open. In this case, an interaction between continuous and discrete states takes place which leads to regular structures in the continuous spectrum. If several channels are open, continuum-continuum interactions may occur. The theoretical formalism in this case is analogous. For an open channel, the effective quantum number is replaced by a phase shift [28] which is implicitly defined by Eq. (15) as a function of the energy W. The intensities can be calculated from the transition moments in the eigenchannel basis and the amplitudes of the wave functions.

D. Two-channel quantum-defect theory

The photoionization spectrum with final-state angular momentum $N=2$ is dominated by the rotational interaction between p Rydberg series built on the $(1,0)\{1,0^0\}$ and $(3,0)\{1,0^0\}$ cores, respectively (see Fig. 2). This interaction is apparent from the pronounced Beutler-Fano profiles in the region between the two thresholds [Fig. 3(b)] and the corresponding intensity modulation in the region below the $N^+=1$ threshold [Fig. 3(a)]. Hence we restrict the analysis to a two-channel quantum-defect model which permits a direct comparison of the experimentally determined parameters with the theoretical frame transformation angle and *ab initio* quantum-defect functions.

In the case of two ionization channels with ionization limits I_1 and I_2, the frame transformation matrix $U_{i\alpha}$ in Eq. (9) can be used, and Eq. (15) simplifies to

$$\tan\pi[-\nu_1(W)-\overline{\mu}]-c_1+\frac{c_2}{c_1-\tan\pi[\nu_2(W)+\overline{\mu}]}=0, \quad (16)$$

with the abbreviations $\overline{\mu}=(\mu_{\alpha1}+\mu_{\alpha2})/2$, $\delta=\mu_{\alpha1}-\mu_{\alpha2}$, $c_1=\tan(\delta\pi/2)\cos(2\theta)$, and $c_2=(\tan(\delta\pi/2)\sin(2\theta))^2$, the eigenchannel quantum defects $\mu_{\alpha1}$ and $\mu_{\alpha2}$, and the frame transformation angle θ. The equation gives an implicit dependence between the quantum numbers ν_1 and ν_2. The Rydberg equation

$$W\equiv I_1-\frac{R}{\nu_1^2}=I_2-\frac{R}{\nu_2^2} \quad (17)$$

determines the energies W of the eigenvalue spectrum. Equation (16) is periodic modulo 1 in ν_1 as well as in ν_2. This property leads us to a graphical solution of the problem [28,30]. For each experimentally observed level with energy W, we determine the effective quantum numbers ν_1 and ν_2 with respect to both ionization thresholds I_1 and I_2 according to Eq. (17), and the quantum defect $\mu=n-\nu_1$ with integer n. In a plot of μ versus ν_2, the data points form characteristic branches, and the locations of the perturbations can be easily recognized in the plot. If ν_2 modulo 1 is used as the abscissa (Lu-Fano plot), the branches collapse to a single curve, and the properties of the molecular system can be extracted immediately [28]. The intersections of the experimental data points in the Lu-Fano plot with the paradiagonal $\mu=1-\nu_2$ give the eigenchannel quantum defects $\mu_{\alpha1}$ and $\mu_{\alpha2}$. For the frame transformation angle θ, the relation

$$\cot^2\theta=\left(\frac{\partial\mu}{\partial\nu_2}\right)_{\nu_2=-\mu_{\alpha2}} \quad (18)$$

can be derived. The amplitudes $B_{\alpha1}$ and $B_{\alpha2}$, calculated from Eq. (14), are

$$B_{\alpha1}(\nu_2)=-\sin\pi[\mu_{\alpha2}+\nu_1(\nu_2)]/\sin\pi\delta\cos\theta, \quad (19)$$

$$B_{\alpha 2}(\nu_2)=\sin\pi[\mu_{\alpha 1}+\nu_1(\nu_2)]/\sin\pi\delta\sin\theta. \quad (20)$$

Having the amplitudes of the wave functions, the intensities in the Beutler-Fano region and in the discrete part of the spectrum are given by

$$I(\nu_2)=[D_{\alpha 1}B_{\alpha 1}(\nu_2)+D_{\alpha 2}B_{\alpha 2}(\nu_2)]^2 \quad (21)$$

and

$$I(\nu_2)=[D_{\alpha 1}B_{\alpha 1}+D_{\alpha 2}B_{\alpha 2}]^2 \Big/ \left[\nu_1^3+\left(\frac{\partial\mu}{\partial\nu_2}\right)\nu_2^3\right], \quad (22)$$

respectively, with the matrix elements of the electronic transition moment, $D_{\alpha 1}$, and $D_{\alpha 2}$, in the eigenchannel basis. The denominator in Eq. (22) arises from the normalization factor and includes the derivative of the function $-\nu_1(\nu_2)$ which has maxima close to energies of the series converging to the higher ionization limit. This interaction produces the typical intensity windows observed in the discrete spectrum.

Equation (15) has some properties which should be noted. For simplicity, they are described in a two-channel case.

(1) The spectrum depends only on a few parameters, given by I_1, I_2, $\mu_{\alpha 1}$, $\mu_{\alpha 2}$, and θ, which can all be determined from experiment (see the Appendix of Ref. [28]).

(2) Solving Eq. (15) in the limit of $\mu_{\alpha 1}\rightarrow\mu_{\alpha 2}$, the spectrum converges to that of the unperturbed $\mu_{\alpha 2}$ series. The physical meaning of this is that the colliding electron ''sees'' an isotropic core which cannot cause any mixing.

(3) In the limit $\theta\rightarrow 0$, the frame transformation matrix $U_{i\alpha}$ becomes a unit matrix. The eigenchannel basis converges to the ionization channel basis. As a result, the equation system breaks up into N single-channel problems having individual quantum defects. The coupling strength is monotonically increasing with the value of θ. For $\theta=\pi/2$ the $U_{i\alpha}$ matrix has only off-diagonal elements, meaning that both series appear unperturbed but interchange their quantum defects.

VI. TWO-CHANNEL ANALYSIS

As discussed in Sec. III and shown in Fig. 2, the electronic symmetries of pure p states in Hund's case (b) are A_2'' and E'. Neglecting perturbations from different vibrational channels other than $\{1,0^0\}$, two eigenchannel quantum defects $\mu_{A_2''}$, and $\mu_{E'}$ have to be specified for solving Eq. (15). In this approximation, the $N=0$ and 1 series have pure electronic symmetries A_2'' and E', respectively, and should appear unperturbed. For $N=2$, both electronic symmetries are allowed leading to rotational interaction. In the following, we apply a two-channel model to fit the discrete lines of the $N=2$ series.

A. Rydberg series with $N=0$ and 2

1. Discrete spectrum

For the discrete lines with final-state angular momentum $N=0$ and 2 (see Sec. IV), we calculated the effective quantum numbers ν_1 and ν_3 with respect to the ionization limits

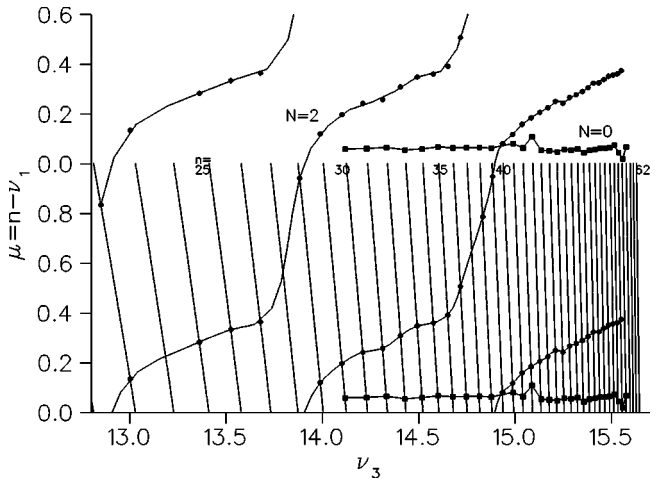

FIG. 5. Two-channel quantum-defect analysis of the discrete lines with $N=0$ and 2 final-state angular momentum. The quantum defect $\mu=n-\nu_1$ with respect to the $(N^+=1,\ G^+=0)$ threshold is plotted vs the effective quantum number ν_3 with respect to the $(N^+=3,\ G^+=0)$ threshold of symmetric-stretch-excited $H_3^+\{1,0^0\}$. The ionization limits listed in Table I are used. The data points for $N=0$ and 2 are displayed by squares and circles, respectively. Lines connecting the data points are drawn to guide the eye. The dependence between μ and ν_3 established by the Rydberg equation (17) is shown as a set of lines labeled by the integer values of the principal quantum number n.

$(N^+=1,\ G^+=0)$ and $(N^+=3,\ G^+=0)$ of symmetric-stretch-excited H_3^+ listed in Table I. (The subscripts 1 and 3 refer to the quantum numbers $N^+=1$ and 3 of the ionization thresholds). In Fig. 5, the quantum defect $\mu=(n-\nu_1)$ is plotted versus the effective quantum number ν_3. For orientation, the relation between ν_1 and ν_3 established by the Rydberg equation (17) is shown as a set of thin lines in Fig. 5.

The data points of the p Rydberg series with angular momentum $N=0$ show a constant quantum defect μ with two minor irregularities. The line positions can be fitted by a simple Rydberg formula. We find an ionization threshold of $12\,831.10\pm 0.01$ cm^{-1}, in excellent agreement with the $(N^+=1,G+=0)\{1,0^0\}$ threshold listed in Table I and a quantum defect of 0.0602 ± 0.001. In contrast to this, the lines of the series with $N=2$ follow monotonically increasing branches. Three perturbers belonging to the $N^+=3$ threshold are clearly recognized in the spectral range investigated. In Fig. 6, the state energies with $N=2$ are shown in a $(\mu=n-\nu_1)$ versus (ν_3 modulo 1) plot (Lu-Fano plot). Now the three different branches seen in Fig. 5 collapse, forming two monotonically increasing curves. The thick solid lines represent the implicit relation between ν_1 and ν_3 of Eq. (16). The optimum fit to the experimental points is achieved for the values $\mu_{A_2''}=0.0599$, and $\mu_{E'}=0.397$ of the eigenchannel quantum defects, and a frame angle of $\theta=0.880$. The results are listed in Table II. The frame transformation angle θ agrees extremely well with the theoretical value $\theta=\arccos(\sqrt{2/5})\approx 0.8861$ derived in Sec. V B. The quantum defects $\mu_{A_2''}$ and $\mu_{E'}$ of vibrationally excited H_3 are slightly higher than the corresponding values for vibrationless H_3 measured by Bordas *et al.* [19]. The theoretical quantum defects listed in Table II were calculated recently by

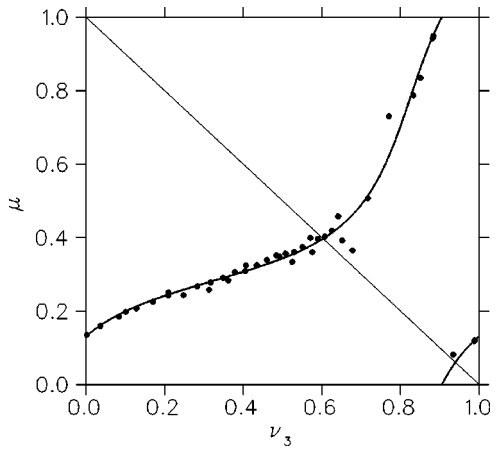

FIG. 6. Lu-Fano plot of the discrete lines with $N=2$. The effective quantum defect μ is plotted as a function of the effective quantum number ν_3 modulo 1. The solid line represents the implicit relation between μ and ν_3 established by the two-channel quantum-defect equation (16). The eigenchannel quantum defects $\mu_{A_2''}$, and $\mu_{E'}$ and the frame transformation angle θ were varied for optimum fit to the data points while keeping the thresholds I_1 and I_3 fixed. The fit parameters are listed in Table II.

Jungen [33] using the pseudo-natural-orbitals method.

Considering the high accuracy of the experimental and theoretical data, the agreement between the experimental values for symmetric-stretch-excited H_3 and the theoretical values for equilibrium geometry is not satisfying at first. The discrepancies cannot be attributed to the weak dependence of the quantum defects on the principal quantum number n. However, the *ab initio* quantum defects depend sensitively on the nuclear configuration. For a comparison between theory and experiment, we therefore calculated the eigenchannel quantum defects $\mu_{\nu,\Gamma}$ by integrating [34,21] over the *ab initio* quantum-defect surface $\mu_\Gamma(Q)$ [33],

$$\tan \pi\mu_{\nu,\Gamma} = \int_{-\infty}^{\infty} d^3Q \chi_\nu^+(Q) \tan[\pi\mu_\Gamma(Q)] \chi_\nu^+(Q), \tag{23}$$

which was expanded in normal coordinates Q. For the calculation of the $np\mu_{A_2''}$, we used the vibrational wave function $\chi^+_{\{1,0^0\}}(Q)$ of symmetric-stretch-excited H_3^+, and integrated over the three normal coordinates. To avoid complications by Jahn-Teller splitting, integration was restricted to the symmetric-stretch normal coordinate to calculate the $np\mu_{E'}$ eigenchannel quantum defect. These *ab initio* expectation values for the eigenchannel quantum defects are listed in the last column of Table II. They agree extremely well with the experimental data.

2. Beutler-Fano spectrum

The photoionization spectrum in the region between the $(N^+=1, G^+=0)$ and $(N^+=3, G^+=0)$ ionization limits recorded with parallel polarization vectors of the lasers is shown in Fig. 7. The regular modulations in the continuum are characteristic for the presence of an open channel and a closed channel. The channel mixing between $N=2$ Rydberg states converging to the $N^+=1$ and 3 thresholds already observed in the discrete spectrum extends into the Beutler-Fano region. The process can be viewed as a rotational autoionization of the $N=2$ series from a bound state of the $N^+=3$ series into the continuum of the $N^+=1$ series. The dip widths represent the lifetimes of the discrete states which are of the order of some hundred fs. The two-channel model is applied by replacing $-\pi\nu_1$ by a continuous phase shift τ, and solving Eq. (16) analytically as a function $\tau(\nu_3)$ using the eigenchannel quantum defects already determined. We

TABLE II. Quantum defects, frame transformation angle, and ionization limits observed in this work for the symmetric-stretch-excited np Rydberg series of H_3.

	Experimental $\{1,0^0\}$[a]			$\{0,0^0\}$[b]	Theoretical	
	$N=0$	$N=1$	$N=2$		at equilibrium[c]	$\chi^+_{\{1,0^0\}}$ weighted[d]
$np\ \mu_{A_2''}$	0.0602		0.0599	0.05	$n=4$: 0.0701 $n=5$: 0.0700	$n=4$: 0.0619
$np\ \mu_{E'}$		0.389	0.397	0.39	$n=4$: 0.3869 $n=5$: 0.3819	$n=4$: 0.3976
$nd\ \mu_{E'}$		0.067 $n=3$: 0.049[e]				
$\theta(N=2)$			0.880		$\arccos(\sqrt{2/5})=0.8861$	
$\theta(N=1)$		0.181				
	$I_{N^+=1}=12\,831.10\ \text{cm}^{-1}$ $I_{N^+=3}=13\,250.58\ \text{cm}^{-1}$ $I_{N^+=3}-I_{N^+=1}=419.48\ \text{cm}^{-1}$				$I_{N^+=3}-I_{N^+=1}=419.475\ \text{cm}^{-1}$[f]	

[a]This work. We estimate the uncertainties of the quantum defects to be ± 0.001.
[b]Analogous values for the vibrationless np series measured by Bordas *et al.* [19].
[c]*Ab initio* quantum defects of np states in H_3 equilibrium configuration [33].
[d]Weighted over the *ab initio* quantum-defect surface using the vibrational wave function of symmetric-stretch-excited $H_3^+\{1,0^0\}$.
[e]Quantum defect of the H_3 $3d\ E'\ (1,3)\{0,0^0\}$ state [35].
[f]*Ab initio* data of Ref. [25].

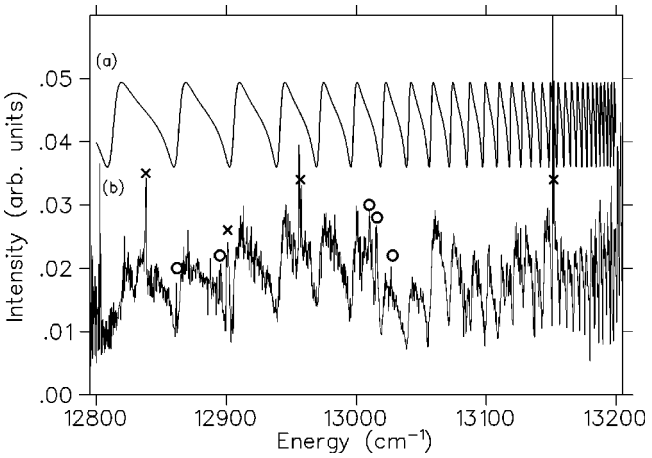

FIG. 7. Photoionization spectrum of symmetric-stretch-excited $H_3\{1,0^0\}$ p Rydberg states in the Beutler-Fano region between the $(N^+=1,\ G^+=0)$ and $(N^+=3,\ G^+=0)$ thresholds. A comparison between theoretical (a) and experimental (b) spectra in the energy region 12 790–13 210 cm^{-1} above the $3s\ ^2A_1'(N=1,\ G=0)\{1,0^0\}$ intermediate state is shown. The experimental spectrum was measured with parallel orientation of the laser polarization vectors. The theoretical curve is shifted vertically by 0.036 for clarity of presentation. Strong resonances from vibrational interloper states are marked by $\times$. Additional weaker resonances marked by $\bigcirc$ become more clearly visible on an enlarged intensity scale.

calculated the amplitudes from Eqs. (19) and (20) and the photoion intensity from Eq. (21). Optimum agreement between the calculated photoion intensity and the measured curve was achieved for a ratio of the transition moments $D_{A_2''}/D_{E'}=1.41$, with an estimated uncertainty of ± 0.3. The theoretical spectrum shown in Fig. 7(a) oscillates between zero (shifted to intensity 0.036 in Fig. 7) and a constant intensity and reproduces all the periodic structures in the measured spectrum [Fig. 7(b)]. In the experiment the autoionization spectrum of the $N=2$ states is superimposed on the continua of the symmetric-stretch-excited $N=0$ series and on the underlying vibrationless and degenerate-mode excited open ionization channels. Therefore, the minima of the experimental curve do not reach the zero level of the intensity scale. The marked deviation of the experimental spectra near 13 040 cm^{-1} is attributed to an instability of the laser power.

The ratio of the transition moments $D_{A_2''}/D_{E'}=1.41$ used to fit the experimental data is appreciably larger than the ratio $D_{A_2''}/D_{E'}=(\sqrt{4/45}/\sqrt{2/15})\approx 0.82$ used by Bordas *et al.* [19] to model the Beutler-Fano region of vibrationless H_3. Bordas *et al.* [19] calculated the ratio of the transition moments from angular momentum considerations in the united-atom approximation assuming the pure electronic transition moment T_{el} to be independent of the electronic symmetry. This assumption is inappropriate. We find that the larger ratio of the transition moments $D_{A_2''}/D_{E'}=1.41$ found here would appreciably improve the agreement between measurement and calculation in the Beutler-Fano region shown in Ref. [19]. In order to explore this subject further we calculated the electronic eigenchannel transition moments from the $3s$ state to the $15p\alpha$ $(\alpha=A_2'',E')$ states by numerically integrating the dipole transition formula

$$T^{(el)}_{3sA_1'\to 15p\alpha}=\int_0^\infty dr\ \rho_{\nu_f 15p\alpha}(r)\, r\, \rho_{\nu_i 3sA_1'}(r),\quad \alpha=A_2'',E', \tag{24}$$

using the solutions of the radial Schrödinger equation

$$\rho_{\nu l\Gamma}=f_{\nu l}(r)\cos(\pi\mu_\Gamma)-g_{\nu l}(r)\sin(\pi\mu_\Gamma). \tag{25}$$

For the $3s\ ^2A_1'$ state, we use $l=0$, $\mu_{3sA_1'}=0.067$, and $\nu=3-\mu_{3sA_1'}=2.933$. For the $15p\alpha$ states, we have $l=1$ and the effective quantum numbers $\nu=15-\mu_\alpha$ determined from the eigenchannel quantum defects μ_α listed in Table II. The r integration was carried out in the region between 0.5 and 40 bohr. We find a ratio of

$$\frac{D_{A_2''}}{D_{E'}}\equiv\frac{\sqrt{4/45}T^{(el)}_{3sA_1'\to 15pA_2''}}{\sqrt{2/15}T^{(el)}_{3sA_1'\to 15pE'}}=1.14 \tag{26}$$

between these transition moments. The value calculated here falls outside the stated uncertainty of the fitted value. Therefore, we calculated geometry-dependent dipole transition moments $T^{(el)}(Q)$ from the *ab initio* quantum-defect surface [33]. We weighted the expanded function $T^{(el)}(Q)$ with the vibrational wave function by an expression similiar to formula (23). The weighting changes the amplitude ratio by 1% compared to the ratio in equilibrium configuration, and cannot be responsible for the disagreement with the experiment.

Several resonance features appear in the spectral region shown in Fig. 7 which are not part of the two-channel modulation of the ionization spectrum. Four narrow resonances appear at excitation energies of 12 838, 12 901, 12 957, and 13 152 cm^{-1}, marked by $\times$ in Fig. 7. Closer inspection of the spectrum on enlarged intensity scales reveals at least five additional resonances marked by $\bigcirc$ in Fig. 7. The features at 12 957 and 13 152 cm^{-1} are found to have a double-peak structure. All resonances are of similar widths but show quite different intensities. They are attributed to interlopers from higher excited vibrational levels of the H_3^+ core with $N=0$ or 2.

3. Modeling of the spectrum below the $H_3^+\{1,0^0\}$ threshold

In order to test the quality of the two-channel model parameters determined above, we also simulated the ionization spectrum below the threshold. The intensity of the ''discrete'' lines was calculated using Eqs. (19) and (22). We combined the fitted eigenchannel quantum defects listed in Table II with the ratio of the transition moments $D_{A_2''}/D_{E'}=1.41$, which we assumed to be energy independent in a range of a few hundred wave numbers around the ionization limits. In Fig. 8, the theoretically calculated spectrum [Fig. 8(a)] is compared with the measured discrete spectrum [Fig. 8(b)] in the 12 695–12 840 cm^{-1} range. The experimental spectrum (a) was measured with parallel polarization of the lasers. Therefore, the lines of the $N=0$ series were included in the calculation. The theoretical stick spectrum was convoluted with a gaussian function of 0.2 cm^{-1} width [full width at half maximum (FWHM)] to take into account the finite laser bandwidth. In the calculated spectrum, the intensity scale is the only adjusted parameter. The agreement between

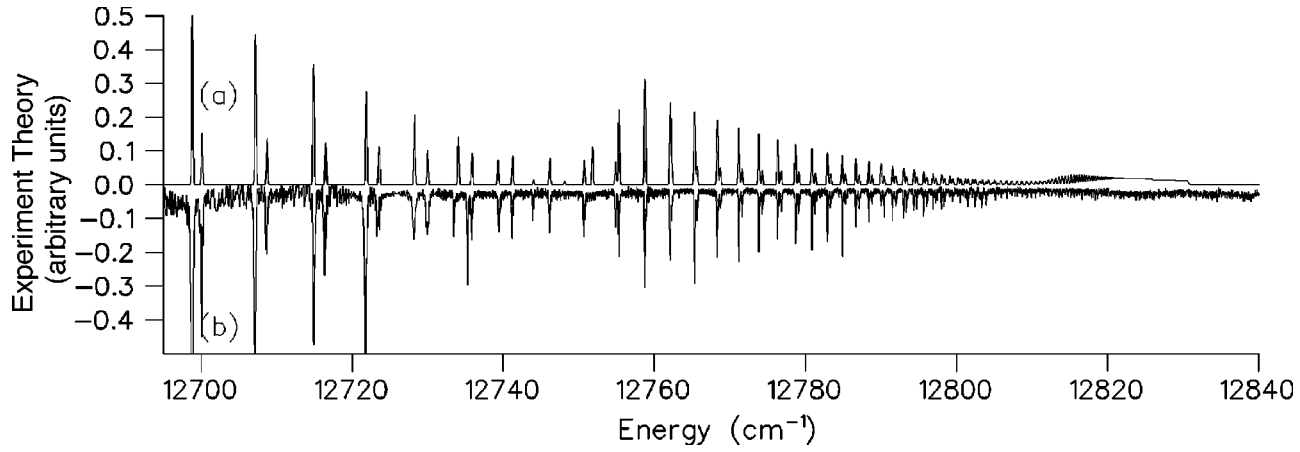

FIG. 8. Comparison between simulated and measured spectra below the $(1,0)\{1,0^0\}$ threshold. The simulated spectrum of the np Rydberg series with total angular momenta $N=0$ and 2 is shown in the 12 695–12 840 cm^{-1} energy range as (a). The ionization thresholds, eigenchannel quantum defects, frame angle, and transition moment ratio listed in Table II were used. The theoretically calculated stick spectrum was convoluted with a Gaussian FWHM 0.2 cm^{-1} width. The experimental spectrum measured with the laser polarizations oriented parallel with respect to each other is shown as (b). A negative scaling factor was applied to the measured spectrum for clarity of presentation.

measured and calculated spectra in Fig. 8 is considered to be extremely good. From the 40 fitted lines, 36 lines are within a deviation of 0.15 cm^{-1}, and all of them agree to better than 0.4 cm^{-1}. This agreement is excellent considering the 0.15 cm^{-1} uncertainty of the excitation energy. In Fig. 9, the effect of the coupling between the two $N=2$ channels is demonstrated. The calculated and experimental spectrum is shown in the 12 710–12 760 cm^{-1} range. The dashed lines at the top of Fig. 9 show the propagation of the spectral line positions from the unperturbed series to the real physical case, when the frame transformation angle is varied from $\theta=0$ to $\theta=\arccos\sqrt{2/5}$. This graphic demonstration of channel interaction provides a rough idea of the mutual shift among energy levels. For $\theta=0$ the $n_3=15$ Rydberg member is nearly degenerate with the $n_1=34$ state. Increasing θ, which is equivalent to increasing the channel interaction, the two states repel each other and this interaction propagates to neighboring n_1 states. While $n_1=31$ is significantly pushed toward lower energy as θ increases, the state $n_1=39$ remains practically constant in energy. This is due to the next higher member of the $N^+=3$ series, $n_3=16$. At the location of $n_1=39$ the interactions due to $n_3=15$ and 16 nearly cancel in their effect on the level position of $n_1=39$.

We note that the $N=2$ level at 12 751.5 cm^{-1} (originally $37p^2A_2''$ in the uncoupled case) is weak in the experimental spectrum probably due to an additional perturbation. An additional feature appears in the measured spectrum in Fig. 9, marked by ○. This line cannot be attributed to the symmetric-stretch-excited $\{1,0^0\}$ p series, and is due to an interloper from a vibrationally highly excited core state. We note that this isolated perturber leads to a significant shift of the $N=2$ line marked by × in Fig. 9.

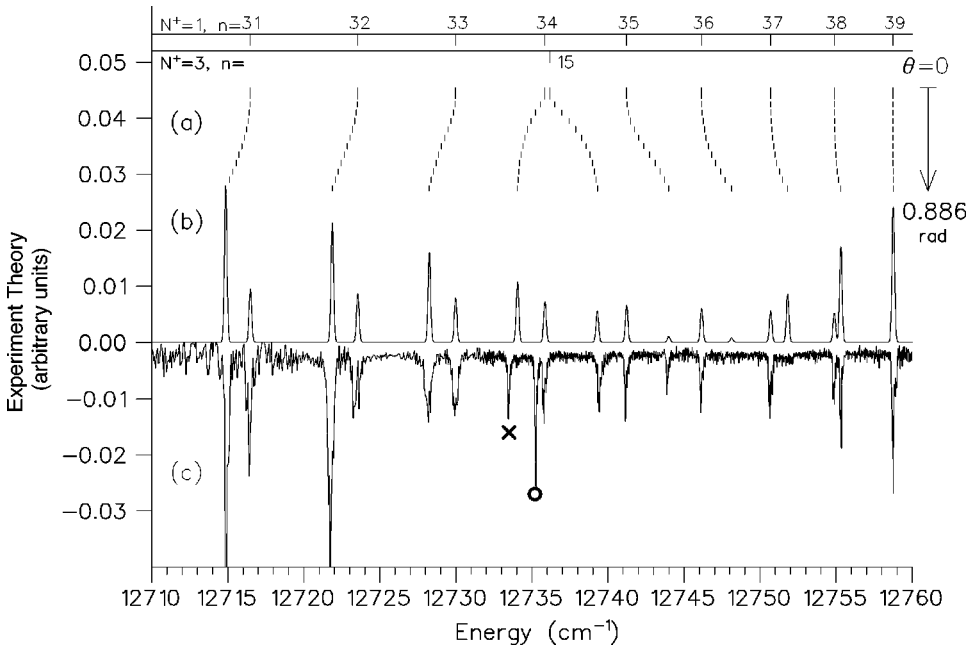

FIG. 9. Close-up spectrum of the $N=2$ lines in the region below the $(1,0)\{1,0^0\}$ threshold. The calculated (b) and measured (c) spectra of the np Rydberg series with $N=0$ and 2 are shown in the 12 710 to 12 760 cm^{-1} range. The low-intensity series belongs to $N=0$. The dashed lines (a) show the propagation of the spectral lines with $N=2$ when turning on the coupling strength from the uncoupled case $\theta=0$ (top) to the theoretical value $\theta=\arccos\sqrt{2/5}$ (bottom). An interloper from a higher vibrationally excited channel marked by ○ leads to a significant shift of the $N=2$ line marked by ×.

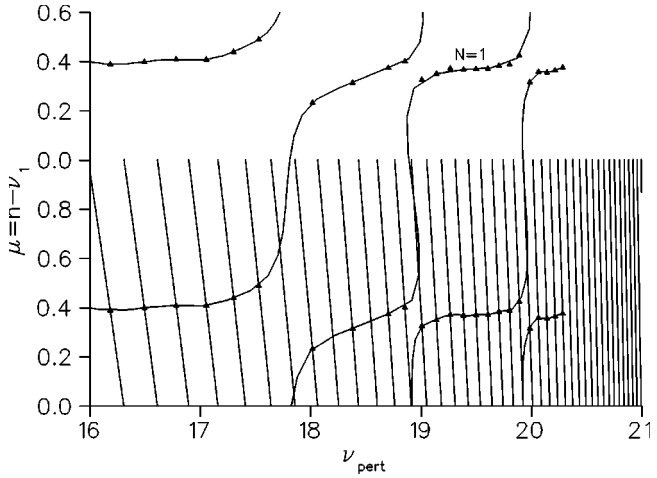

FIG. 10. Two-channel quantum-defect analysis of the discrete lines with final-state angular momentum $N=1$. The quantum defect $\mu = n - \nu_1$ with respect to the $(N^+=1, G^+=0)$ threshold is plotted vs the effective quantum number ν_{pert} with respect to the $(N^+=3, G^+=3)$ threshold of symmetric-stretch-excited $H_3^+\{1,0^0\}$ at 13 053.2 cm^{-1}, as listed in Table III. The lines connecting the data points are drawn to guide the eye along the branches, which are separated from each other by the perturber states.

B. Rydberg series with $N=1$

Unexpectedly we found that the energies of the discrete lines with final-state angular momentum $N=1$ cannot be fitted by a simple Rydberg formula. Three perturbations appear in the spectral range investigated. As discussed in Sec. III, the p Rydberg series with $N=1$ has electronic symmetry E', and cannot be perturbed by other p series built on H_3^+ $(1,0)\{1,0^0\}$ or $(3,0)\{1,0^0\}$ cores. Owing to the periodicity of the observed perturbations and their small spacing, the perturbations must originate from a sequence of Rydberg states belonging to a single rovibrational core state, lying close in energy to the threshold investigated here. We therefore had to consider a change in Rydberg orbital character as a cause of the perturbation. This appreciably increases the number of possible H_3^+ core states. In order to identify the perturbing Rydberg series, we first estimate the ionization threshold I_{pert} by an iterative procedure. For an initial guess of I_{pert}, we draw the experimentally determined energies of the $N=1$ lines in a μ-versus-ν_{pert} plot (Fig. 10). Because of the perturbation, the lines connecting the data points in Fig. 10 form branches. The gaps between the branches are much narrower than those found in the graph of the $N=2$ series in Fig. 5, and the gap width decreases for higher energies. Obviously, the coupling between the channels is much weaker than the rotational coupling observed for the $N=2$ series. The location of each gap corresponds to the effective quantum number of the perturbing state. By adjusting I_{pert}, we can achieve that the gaps appear in distances of $\Delta\nu_{pert} \approx 1$. The values of I_{pert} consistent with the experimental data are restricted to the interval $13\,080 \pm 80$ cm^{-1} which falls *between* the $(N^+=1, G^+=0)\{1,0^0\}$ and $(N^+=3, G^+=0)\{1,0^0\}$ thresholds.

Table III lists all H_3^+ levels in the energy range between 13 000 and 13 160 cm^{-1} above the H_3 $3s\ ^2A_1'(1,0)\{1,0^0\}$ state. These energies were determined in highly accurate *ab initio* calculations [25]. Due to the applied two-step excitation scheme, the rovibronic symmetry of the final state has to be A_2'', as discussed in Sec. III. Hence the rovibrational symmetry of the underlying H_3^+ core in the final state has to be A_2' for L odd and A_2'' for L even. In addition, the quantum number G^+ has to be an integer multiple of 3. The only A_2' candidate state in Table III is $(N^+=5, G^+=3)\{0,1^1\}$ for L odd. In order to construct $N=1$ final states from this core, the (odd) electronic angular momentum quantum number would have to be $L=5$ (h series). Owing to the large change in angular momentum, $\Delta L=4$, this state is unlikely the origin of the observed perturbation. The candidate H_3^+ levels having rovibrational symmetry A_2'' are $(N^+=3, G^+=3)\{1,0^0\}$ and $(N^+=4, G^+=0)\{0,1^1\}$. These cores require (even) electronic angular momenta $L=2$ and 4 and $L=4$, respectively, to construct a total angular momentum $N=1$. The choice with lowest value of L is the $(N^+=3, G^+=3)\{1,0^0\}$ state. Additionally, this core has the same vibrational excitation as the perturbed p-series which enhances the Franck-Condon factor in the coupling matrix element. The combination of the H_3^+ $(N^+=3, G^+=3)\{1,0^0\}$ state with a d electron $(L=2)$ leads to the $nd(1,3)\{1,0^0\}$ series of H_3. In the Hund's case (b) frame, this series has a projection $\lambda = 2$ of the electronic angular momentum $L=2$ onto the top axis and, therefore, E' electronic symmetry identical to the electronic symmetry of the perturbed $N=1$ series.

In the μ-versus-ν_{pert} plot (Fig. 10), the ionization limit 13 053.2 cm^{-1} of the $(N^+=3, G^+=3)\{1,0^0\}$ core listed in Table III was used. We fitted the experimental data of the $N=1$ series by a two-channel QDT model according to Eq.

TABLE III. Possible H_3^+ core states for the perturber of the np Rydberg series with $N=1$ in the energy range 13 000–13 160 cm^{-1} above the $3s\ ^2A_1'(1,0)\{1,0^0\}$ intermediate state. The core states of the np Rydberg series studied here are also given in the first and last lines of the table.

$(N^+, G^+)\{\nu_1, \nu_2^l\}$	U[a]	s[b]	Energy[c]	$\Gamma_{H_3^+}$	Threshold[d]	L[e]
$(1,0)\{1,0^0\}$	0		3262.997	A_2'	12 831.10	1
$(2,1)\{1,0^0\}$	0		3409.661	E''	12 977.761	
$(2,0)\{1,0^0\}$	0		3431.728	A_1'	12 999.828	
$(3,3)\{1,0^0\}$	0	± 1	3485.115	A_1'', A_2''	13 053.215	2,4
$(3,2)\{1,0^0\}$	0		3595.514	E'	13 163.614	
$(4,1)\{0,1^1\}$	1		3422.634	E'	12 990.734	
$(4,0)\{0,1^1\}$	1		3446.555	A_1'', A_2''	13 014.655	4
$(5,4)\{0,1^1\}$	1		3509.629	E''	13 077.729	
$(5,3)\{0,1^1\}$	-1	± 1	3552.822	A_1', A_2'	13 120.922	5
$(5,)\{\}$[f]			3554.247		13 122.347	
$(3,0)\{1,0^0\}$	0		3682.472	A_2'	13 250.58	3

[a]Defined by $|U| = |l_2|$ (l_2 is the quantum number of the vibrational angular momentum). The sign of U is + or − for the upper and lower levels of the l doubling, respectively.

[b]The Wang index $s = \pm 1$ is defined for $G=3$ and describes, the splitting of A_1 and A_2 levels.

[c]Energy in cm^{-1} from the *ab initio* calculation [25], relative to the minimum of the potential-energy surface.

[d]Energy in cm^{-1} above the $3s\ ^2A_1'(1,0)\{1,0^0\}$ intermediate state.

[e]Possible angular momentum L of the Rydberg electron for the total angular momentum $N=1$, taking into account the symmetry analysis discussed in Sec. III.

[f]Assignment unknown.

(16) with a threshold fixed to $I_{\mathrm{pert}}=13\,053.2\ \mathrm{cm}^{-1}$ and the eigenchannel quantum defects and the frame transformation angle as free parameters. An optimum fit was achieved with the values $\mu_{npE'}=0.389$, $\mu_{ndE'}=0.067$, and $\theta=0.181$. The value of $\mu_{npE'}$ agrees extremely well with that found in the analysis of the $N=2$ series. Our fitted value $\mu_{ndE'}=0.067$ applies to the $(n=18\ldots20)d$ states of the $(N^+=3,\ G^+=3)\{1,0^0\}$ core, and is reasonably close to the quantum defect of the $3dE'(1,3)\{0,0^0\}$ state $\mu=0.049$ which has a $(N^+=3,\ G^+=3)\{0,0^0\}$ core [35].

Due to the change in electronic angular momentum, the frame transformation angle cannot be calculated analytically as is the case in pure rotational coupling. The channel coupling between the np series with a $(N^+=1,\ G^+=0)$ core and the nd series with a $(N^+=3,\ G^+=3)$ core is quite surprising, and to our knowledge has never previously been reported. In terms of a collision picture, the core angular momentum N^+ as well as its projection on the molecular top axis K^+ are changed back and forth between $(N^+=1,\ K^+=0)$ and $(N^+=3,\ K^+=3)$ by the impact of the valence electron which switches between p and d character. The enormous mass difference of the ion core and the outer electron causes this process to be only a small perturbation.

C. Continuum

In our two-channel model, the pure continuum starting above the $(N^+=3,\ G^+=0)$ limit at $13\,250.58\ \mathrm{cm}^{-1}$ should be structureless, and should not vary with the photon energy. The measured spectrum in the $13\,250$–$14\,200\ \mathrm{cm}^{-1}$ region is shown in Fig. 3(c). During the comparatively long duration of the data acquisition ($\sim$60 h), it is a challenge to guarantee stable operating conditions for the apparatus. The drop in the overall signal level around $13\,800\ \mathrm{cm}^{-1}$ may be due to an instability of the ion-beam alignment. Apart from this, we observe an almost structureless continuum with only isolated resonances produced by interloper states from higher vibrationally excited H_3^+ ion cores. Some resonances appear as broad features with peak widths of more than $7\ \mathrm{cm}^{-1}$ FWHM. Others are narrow lines and the peak structure becomes visible on expanded energy scales shown in the two insets in Fig. 3(c). A few resonances show strongly asymmetric, Fano-type line profiles [27] with negative as well as positive values of the shape-defining profile index q. The appearance of these resonances shows no regular pattern and an assignment is beyond the scope of this investigation. The features in the continuum will be investigated by multichannel quantum-defect theory in a forthcoming publication from this laboratory [36].

VII. CONCLUSION

We investigated vibrationally symmetric-stretch excited np Rydberg states of H_3 with angular momenta $N=0$, 1, and 2. The np Rydberg series with $N=0$ is unperturbed and can be described by a simple Rydberg formula. Two rotationally coupled np series with $N=2$ were analyzed using a two-channel quantum-defect method. The eigenchannel quantum defects of the p states with electronic symmetries A_2'' and E' and the frame transformation matrix were determined. The observed values of the eigenchannel quantum defects are in very good agreement with the results of *ab inito* quantum-defect surfaces. The eigenchannel quantum defects and the frame transformation angle from the analysis were used to simulate the spectrum in the discrete region as well as the Beutler-Fano region. The ratio of the transition moments from the $3s\ ^2A_1'$ to the $np\ A_2''$ and $np\ E'$ states was found to be $D_{A_2''}/D_{E'}=1.41$. A theoretical determination of the latter could explain the tendency but not exactly reproduce the experimental value within the estimated uncertainty. The simple two-channel description explains the observed line positions and intensity windows in the spectra with high accuracy. The discrepancies between the calculated and observed line positions are generally smaller than $0.15\ \mathrm{cm}^{-1}$ except for some isolated lines, which are additionally perturbed by nearby interloper states of higher vibrationally excited series.

Surprisingly, the series with $N=1$ final-state angular momentum was found to be perturbed. By energy, angular momentum, and symmetry arguments, the nd Rydberg series with E' electronic symmetry built on a symmetric-stretch-excited $(N^+=3,\ G^+=3)\{1,0^0\}$ H_3^+ core was identified as the perturber. In a collision picture, the perturbation must be viewed as a collision of the valence electron which changes the rotation axis of the heavy ion core. Therefore, the coupling strength is small but clearly noticeable in the line positions and intensities in the spectra.

Resonances from interloper states with vibrationally higher excited H_3^+ cores were observed in the ''discrete''region, the Beutler-Fano region, and the pure continuum. The assignment of these penetrating vibrational interloper states is a topic of further investigations using multichannel quantum-defect theory.

ACKNOWLEDGMENTS

We are indebted to Professor M. Jungen (University of Basel) for performing *ab initio* calculations of the quantum defect for the states of H_3 relevant for this work. We would like to thank Professor R. Jaquet (University of Siegen) for many fruitful discussions and for making the results of his *ab initio* calculations of the H_3^+ rovibrational levels available to us. We are grateful for many discussions with Dr. J. Stephens (IAEA, Wien). Thanks must go to U. Person and A. Holzer for their technical help during construction and operation of the apparatus. This research was supported by Deutsche Forschungsgemeinschaft (SFB 276 TP C13).

[1] A. Kuppermann and Y.-S. M. Wu, Chem. Phys. Lett. **241**, 229 (1995).

[2] L. Schnieder, K. Seekamp-Rahn, J. Borkowski, E. Wrede, K. H. Welge, F. J. Aoiz, L. Bañares, M. J. D'Mello, V. J. Herrero, V. S. Rábanos, and R. E. Wyatt, Science **269**, 207 (1995); L. Bañares, F. J. Aoiz, V. J. Herrero, M. J. D'Mello, B. Niederjohann, K. Seekamp-Rahn, E. Wrede, and L. Schnieder, J. Chem. Phys. **108**, 6160 (1998).

[3] J. B. A. Mitchell, J. L. Forand, C. T. Ng, D. P. Levac, R. E. Mitchell, P. M. Mul, W. Claeys, A. Sen, and J. Wm. McGowan, Phys. Rev. Lett. **51**, 885 (1983).
[4] J. B. A. Mitchell, Phys. Rep. **186**, 215 (1990).
[5] S. Datz, G. Sundstrom, Ch. Biedermann, L. Brostrom, H. Danared, S. Mannervik, J. R. Mowat, and M. Larsson, Phys. Rev. Lett. **74**, 896 (1995).
[6] G. Herzberg, J. Chem. Phys. **70**, 4806 (1979).
[7] I. Dabrowski and G. Herzberg, Can. J. Phys. **58**, 1238 (1980).
[8] G. Herzberg and J. K. G. Watson, Can. J. Phys. **58**, 1250 (1980).
[9] G. Herzberg, H. Lew, J. J. Sloan, and J. K. G. Watson, Can. J. Phys. **59**, 428 (1981).
[10] G. Herzberg, J. T. Hougen, and J. K. G. Watson, Can. J. Phys. **60**, 1261 (1982).
[11] F. M. Devienne, C.R. Acad. Sci. Paris **267**, 1279 (1968).
[12] G. I. Gellene and R. F. Porter, J. Chem. Phys. **79**, 5975 (1983).
[13] H. Helm, L. J. Lembo, P. C. Cosby, and D. L. Huestis, *Fundamentals of Laser Interaction II*, edited by F. Ehlotzky, Lecture Notes in Physics Vol. 1339 (Springer-Verlag, Berlin, 1989), p. 264.
[14] H. Helm, Phys. Rev. Lett. **56**, 42 (1986).
[15] H. Helm, Phys. Rev. A **38**, 3425 (1988).
[16] L. J. Lembo and H. Helm, Chem. Phys. Lett. **163**, 425 (1989).
[17] P. C. Cosby and H. Helm, Phys. Rev. Lett. **61**, 298 (1988).
[18] L. J. Lembo, M. C. Bordas, and H. Helm, Phys. Rev. A **42**, 6660 (1990).
[19] M. C. Bordas, L. J. Lembo, and H. Helm, Phys. Rev. A **44**, 1817 (1991).
[20] Ch. Nager and M. Jungen, Chem. Phys. **70**, 189 (1982).
[21] J. A. Stephens and Chris H. Greene, Phys. Rev. Lett. **72**, 1624 (1993); J. Chem. Phys. **102**, 1579 (1995).
[22] U. Müller, U. Majer, R. Reichle, and M. Braun, J. Chem. Phys. **106**, 7958 (1997).
[23] L. J. Lembo, H. Helm, and D. L. Huestis, J. Chem. Phys. **90**, 5299 (1989).
[24] J. T. Hougen, J. Chem. Phys. **37**, 1433 (1962).
[25] R. Jaquet (private communication); W. Cencek, J. Rychlewski, R. Jaquet, and W. Kutzelnigg, J. Chem. Phys. **108**, 2831 (1998); R. Jaquet, W. Cencek, W. Kutzelnigg, and J. Rychlewski, *ibid.* **108**, 2837 (1998).
[26] W. Ketterle, H.-P. Messmer, and H. Walther, Europhys. Lett. **8**, 333 (1989).
[27] U. Fano, Phys. Rev. **124**, 1866 (1961).
[28] U. Fano, Phys. Rev. A **2**, 3535 (1970); **15**, 817 (1977).
[29] Shao-hua Pan and K. T. Lu, Phys. Rev. A **37**, 299 (1988).
[30] C.-M. Lee and K. T. Lu, Phys. Rev. A **8**, 1241 (1973).
[31] M. J. Seaton, Rep. Prog. Phys. **46**, 167 (1983).
[32] T. F. Gallagher, *Rydberg Atoms* (Cambridge University Press, Cambridge, 1994).
[33] M. Jungen (private communication).
[34] C. Bordas, P. Labastie, J. Chevaleyre, and M. Broyer, Chem. Phys. **129**, 21 (1989).
[35] The $3dE'(1,3)\{0,0^0\}$ state has a pure $(N^+=3,\ G^+=3)\{0,0^0\}$ core and an energy of 17 196.38 cm^{-1} above the $2p\,^2A_2''\ (0,0)\{0,0^0\}$ state [10]. Using the first ionization threshold of the H_3 $2p\,^2A_2''\ (0,0)\{0,0^0\}$ state (2 9562.14 cm^{-1}) [26], and the energies of the $H_3{}^+$ states $(N^+=1,\ G^+=0)\{0,0^0\}$ (86.935 cm^{-1}) and $(N^+=3,\ G^+=3)\{0,0^0\}$ (315.35 cm^{-1}) [25], we find the quantum defect of the H_3 $3dE'$ $(1,3)\{0,0^0\}$ state to be $\mu=0.0484$.
[36] I. Mistrík, R. Reichle, U. Müller, H. Helm, M. Jungen, and J. Stephens, Phys. Rev. A (to be published).
[37] W. Ketterle, H. Figger, and H. Walther, Z. Phys. D **13**, 139 (1989).